Journal of Coastal Life Medicine

journal homepage: www.jclmm.com

Document heading doi: 10.12980/JCLM.3.201514JCLM-2015-0004 ©2015 by the Journal of Coastal Life Medicine. All rights reserved.

Computational fluid dynamics simulation of intracranial aneurysms – comparing size and shape

Zifeng Yang[1*], Hongtao Yu[1], George P. Huang[1], Ryan Schwieterman[2], Bryan Ludwig[2,3]

[1]*Department of Mechanical and Materials Engineering, WrightStateUniversity, Dayton, OH 45435, USA*

[2]*Wright State University Boonshoft School of Medicine, WrightStateUniversity, Dayton, OH 45435, USA*

[3]*Department of Neurology, Division of NeuroInterventional Surgery, WrightStateUniversity / Premier Health, Clinical Neuroscience Institute, 30 E. Apple St, Dayton, OH 45409, USA*

ARTICLE INFO

Article history:
Received 19 Jan 2015
Received in revised form 24 Jan 2015
Accepted 28 Jan 2015
Available online 2 Feb 2014

Keywords:
Intracranial aneurysm
Morphology
Computational fluid dynamics

ABSTRACT

Objective: To study the hemodynamics of an anatomic internal carotid artery aneurysm derived from a patient-specific model and then manipulate into two phantom morphologies: one growing uniformly by size and the other changing shape unevenly.

Methods: The computational model of the saccular, internal carotid artery, aneurysm was constructed from 3D rotational, digitally subtracted, catheter angiography images. Computational fluid dynamics simulations were performed under pulsatile cardiac flow conditions. Velocity vectors, streamlines, pressure, and wall shear stress (WSS) and its variance distributions were quantitatively visualized.

Results: The maximum pressure and WSS from the time-averaged distribution on the inside saccular surface of the original case are 415.38 and 17.61 Pa. In contrast, the bi-lobed shape gives rise to higher peak values of pressure (461.00 Pa) and WSS (33.20 Pa) on the saccular dome. Conversely, the evenly enlarged aneurysm actually results in a slightly lower peak pressure (399.58 Pa) and drastically decreased WSS (9.81 Pa).

Conclusions: The current study indicates that the size of the aneurysm should not be the only determining factor for the rupture risk consideration, the irregularity of the aneurysm shape and the corresponding aberrant hemodynamics might be a more important factor to consider for risk assessment.

1. Introduction

It has been estimated that 3%-7% of the US population harbors an un-ruptured intracranial aneurysm (UIA). There are 35 000 people in the US have an intracranial aneurysm rupture each year[1]. Intracranial aneurysm rupture has devastating effects which include subarachnoid hemorrhage and a 10% mortality rate with 50% mortality within the first month[1]. In addition, the economic impact of subarachnoid hemorrhage is significant with clipping and coiling procedures increasing in cost by approximately $20 000 from 2001 to 2008[2]. Accurate assessment of rupture risks for UIA is a critical factor in medical decision making, but current evidence to guide physicians when counseling patients with UIAs is outdated and incomplete. Most previous methods of predicting aneurysmal rupture of a UIA in the clinical process is based solely on size and location of the aneurysm[3]. Currently, the International Study of Un-ruptured Intracranial Aneurysms (ISUIA) suggests that aneurysms less than 7 mm pose minimal risk for rupture, and therefore surveillance should precede intervention. Surprisingly, our own retrospective reviews (Clinical Neuroscience Institute, Wright State University / Premier Health) found that more than half of patients (n=202) who had ruptured intracranial aneurysms were seen to have an aneurysm size of less than 7 mm.

Computational fluid dynamics (CFD) simulations studying the

*Corresponding author: Zifeng Yang, Department of Mechanical and Materials Engineering, WrightStateUniversity, Dayton, OH 45435, USA.

Tel: 1-937-775-5091

E-mail: zifeng.yang@wright.edu

flow in cerebral vasculature and aneurysms has been recognized as an important tool to illuminate the hemodynamic characteristics[4-7]. The risk of rupture of intracranial aneurysms was believed to be associated with the size of the aneurysmal sac and possibly correlated with the shape of the aneurysmal sac in early studies[8]. In recent researches, hemodynamic variables such as wall shear stress (WSS), are believed to play an important role in predicting the rupture of the aneurysmal sac[9-11]. Significant correlations of CFD simulations results with aneurysm formation and rupture risk have been reported in the literature[12-17], unfortunately accurate predictors still remain elusive. The latest review on complex interactions of hemodynamics with intracranial aneurysm initiation, growth and rupture proposed that the high-versus-low WSS is a manifestation of the complexity of aneurysm pathophysiology, and both high and low WSS can drive intracranial aneurysm growth and rupture[18]. The review brought out the hypothesis that low WSS and a high oscillatory shear index can trigger an inflammatory-cell-mediated pathway, which could be associated with the growth and rupture of large, atherosclerotic aneurysm phenotypes, while high WSS combined with a positive WSS gradient can trigger a mural-cell-mediated pathway, which could be associated with the growth and rupture of small or secondary bleb aneurysm phenotypes. The saccular side-wall intracranial aneurysm in the present study belongs to the small bleb aneurysm phenotypes. The current study focuses on the effects of morphology of the bleb aneurysm on the flow pattern within the sac, pressure and WSS distributions on the saccular surface. Based on the hypothesis mentioned above, the rupture risk will be analyzed in correlation with the morphology of the aneurysm.

In the present study, the patient-specific anatomic aneurysmal flow was modeled from the three-dimensional reconstruction of the cerebral vessels using digital subtraction angiographic imaging. According to our retrospective reviews on the previously found aneurysm morphology, uniform growth with conformal shape and remodeling to bi-lobed aneurysm are mostly representative. Therefore, based on the actual three-dimension construction of patient's aneurysm, we have created two phantom scenarios which are believed to increase the likelihood of aneurysmal rupture: (1) increase the size of the aneurysm by approximately two times and (2) create a bi-lobed aneurysm (dysmorphic) by restricting growth at a particular position over the aneurysm surface (mimic of fibrosis of the aneurysmal wall). The hemodynamic characteristics of the two phantom scenarios will be compared with the anatomic model. The present study aims to quantitatively evaluate; (1) the velocity distribution proximal to, and inside of, the aneurysm, (2) pressure distribution on aneurysm surface, (3) the WSS distribution on the surface of the aneurysmal sacs and (4) the variances of pressure and WSS on the saccular surface. While the influence of WSS and pressure is believed to be correlated to the risk management of the aneurysm rupture, the importance of the oscillatory pressure and WSS should not be ignored as the time dependent pulsating behavior of the blood flow may also cause damage to the aneurysm surface. The ultimate goal of the current study is to assess the forces applied to various aneurysms and attempt to extrapolate these with rupture risks for UIAs using computational simulations of intracranial aneurysm hemodynamics.

2. Materials and methods

2.1. Aneurysm characterization

3D digital subtraction angiographic imaging data (Siemens Artis Zee) was obtained from an un-ruptured internal carotid artery (ICA) aneurysm discovered in a 64 year old, Caucasian, female patient with no smoking history or family history of rupture intracranial aneurysms. All 3D imaging was acquired using the Siemens 3D spin software. Images were acquired by careful catheterization of the cervical ICA using a 5F Terumo angle taper catheter and then visipaque 300 contrast agent was injected using the powered injector set at 3 mL/min contrast for 18 mL, total over a 5 second spin with a variable rate rise dependent on the patient's cardiac output and previous digital subtraction angiographic contrast runs. This axial slice data was then collected in DICOM format and de-identified by the operating physician. In this work, 500 slicer image files with the thickness of 0.4 mm were used to reconstruct the 3D blood vessel geometry. The transformation from DICOM format to STL file was performed using a freeware software, 3D-Slicer. The STL file is considered a generic format for both CFD and CAD software.

Figure 1a shows the unmodified 3D vascular reconstruction. As shown in the plot, not only that the data contains a lot of image noise, but there exists many trivial branches associated with various blood vessels. In order to reduce the computation efforts we decided to focus on the regions close to the aneurysm. The modification involves smoothing out the image noise appearing on the vessel surfaces and connections, filling holes, repairing broken connections, and eliminating unwanted small branches (unless they were approaching the ostium or connecting to the aneurysmal sac directly). These modifications can be performed in CAD software or a CFD preprocessor. The final configuration for CFD application is shown in Figure 1b. The ICA aneurysm was classified by two, independent, neurointerventionalist as a side-wall, saccular, unruptured aneurysm exhibiting one lobe. The diameter of the ICA inlet was 5.03 mm, the height of the aneurysm dome is 3.32 mm and the diameter of the aneurysm ostium is 3.72 mm which was comparable to CT angiography measurements. The equivalent inner diameter is calculated as 4.42 mm based on the volume of the aneurysmal sac, which is about 45.19 mm^3.

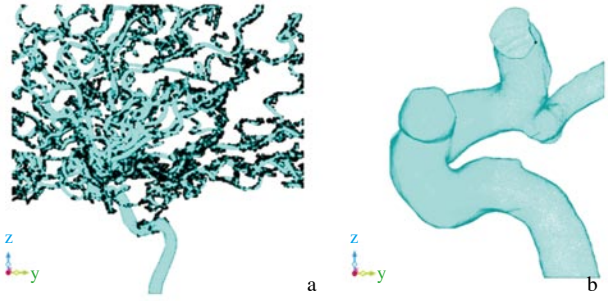

Figure 1. a: Initial 3D model of cerebral arteries; b: Anatomic model after removing noise and arterial branches.

2.2. Aneurysm morphology

In the current study, the original aneurysm acquired from the patient's clinical images was then assumed to evolve in different paths leading to two completely different morphologies, which are considered representative morphologies based on our retrospective review. The initial anatomic model, Figure 2a, was used to perform the transformations using Sculptor Morph V.3.4 (Optimal Solutions Software, LLC.). The first geometry (enlarged) was created by evenly enlarging the aneurysmal sac by 2.1 times which is a reasonable size for observed enlarged aneurysm and it reaches the limit of grid deformation under the current meshing method, as shown in Figure 2b. Compared with the original model, the height from the ostium to the dome was increased to 5.50 mm, the diameter of the ostium was enlarged to 3.89 mm, and the equivalent inner diameter was increased to 5.64 mm. The second model (bi-lobed) was created by restricting the growth on a surrounding curve near to the middle position on the sac surface (like tightening the aneurysmal sac in z direction along the center line), as shown in Figure 2c. The bi-lobed model was assumed to transform from the original anatomic model unevenly while maintaining the maximum diameter of ostium being the same as the original model. As a result, the height from the ostium to the central lowest position of the concave region was reduced to 2.70 mm.

2.3. Computational fluid dynamics

The models can be directly loaded into the commercial CFD software SC/Tetra (Cradle North America, Dayton, OH). The program solves 3D conservation equations of mass and momentum in time (the so-called Navier Stokes equations). As we assume the effect of vessel deformation is small, a rigid wall with no-slip boundary condition was applied to the wall surfaces. Blood was modeled as an incompressible Newtonian fluid with a density of ρ=1 050 kg/m^3 and a dynamic viscosity of μ=4.5×10^3 Pa·s, which is in accordance with previous studies[5,19]. The *in-vivo* measurement of the time-averaged blood flow rate in ICA is approximately 266 mL/min and ICA diameter is around 0.5 cm. This translates into a mean Reynolds number ($Re=\rho VD/\mu$, where V is the averaged velocity in ICA, and D is the diameter of the vessel). Even if we consider the waveform as shown Figure 3, the maximum Reynolds number is merely 816. Therefore, the simulation assumes the flow remains laminar throughout the calculation.

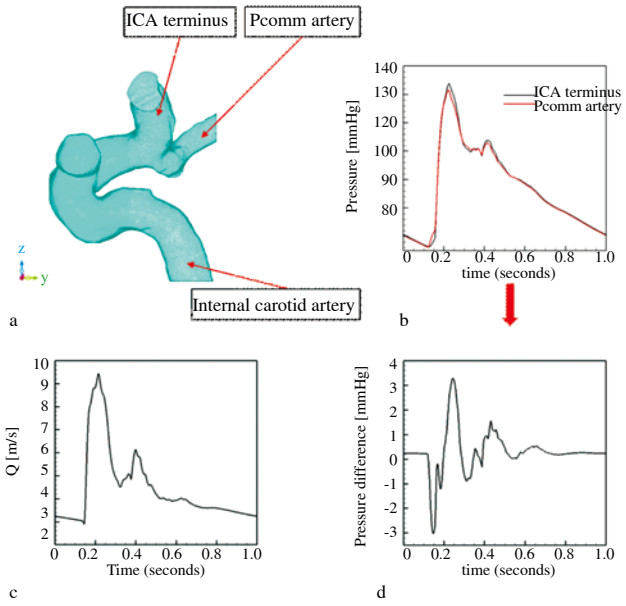

Figure 3. Inlet boundary condition for the simulation: a: Anatomic model; b: Comparison of the pressure waveform for ICA terminus and Pcomm artery; c: Volume flow rate for ICA inlet; d: Pressure difference between ICA terminus and Pcomm artery.

2.4. Simulation parameters

The present study is based on the patient-specific vessel model. Nevertheless, only one mass flow rate waveform was applied at the inlet of ICA. The pulsatile mass inflow rate for the ICA was extracted from a parallel study, in which an in-house computer program for total human intravascular network simulation was developed (published in a separate paper[20]). Blood flow in arteries, capillaries and venules is modeled using lumped parameter models, or the 0D models, which are modeled using the connection of a number of capacitors, resistors and inductors to represent the real biomechanics[21-24]. The simulation results of volume flow rate and pressure are presented in Figure 3c. Compared to the previous study, the outlet pressure boundary condition plays an important role in the mass flow rate working on the aneurysm. Thus, at two distal vessels' outlets, ICA terminus and Pcomm (posterior communicating) artery, a pressure difference wave form was applied for the ICA terminus artery, and a zero-value gage pressure was applied for the Pcomm artery, as shown in Figure 3d. Figure 3b shows the pressure inside the ICA terminus and Pcomm artery. In the current study, five cardiac cycles were performed with a time step of 0.0002

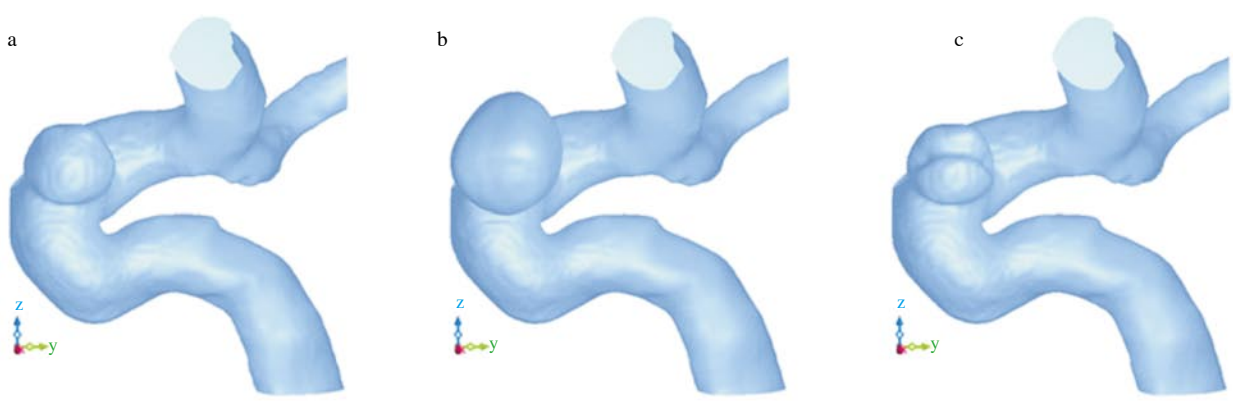

Figure 2. a: Anatomic model and two morphology models; b: Evenly enlarged model; c: Bi-lobed model.

seconds for the coarse mesh and 0.0001 seconds for the fine mesh. The time dependent values of the pressure at the center of aneurysm's ostium, as shown in Figure 4a, are presented in Figure 4b. As can be observed from the plots, a quasi-steady state solution has been reached and therefore all analysis were performed using the solution obtained in the fifth cardiac cycle.

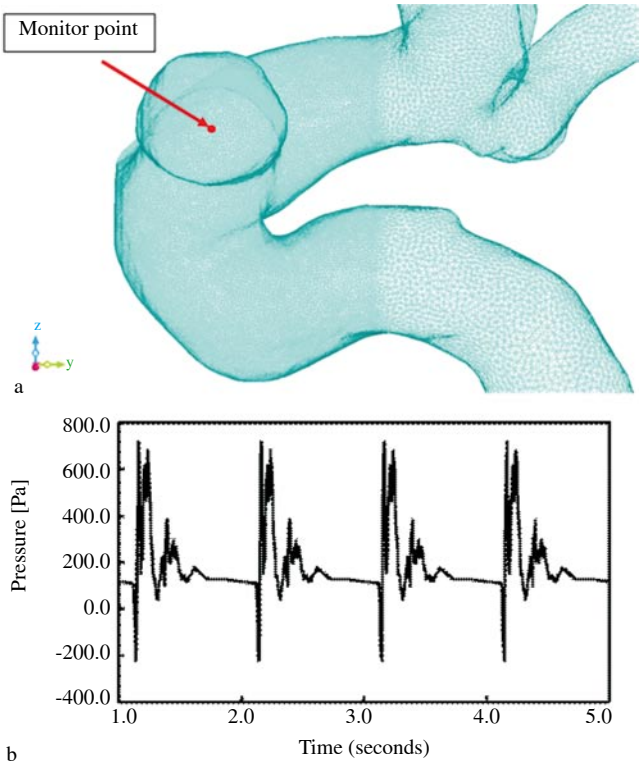

Figure 4. a: The position of monitor point; and b: the corresponding pressure profile from the second period to the fifth period.

2.5. Simulation convergence

To verify the grid convergence, the solutions of two computational meshes were analyzed: 2.5×10^6 and 2.2×10^7 mesh elements. While the increase is only one order of magnitude, the refinement of the grids is mainly concentrated near the aneurysm regions. The execution time for the coarse and fine meshes were 60 h using 8 processors and 380 h using 32 processors, respectively. Time-averaged pressure and WSS acting on the aneurysmal sac surface for the original anatomic case were compared and the results are presented in Figure 5. As can be seen from the contour plots, there is no visual difference between the two calculations and the maximum numerical difference in the averaged pressure and WSS is less than 5% in the two simulations. Hence, the coarse mesh was chosen to conduct the simulation for the rest of this study to simplify and reduce the time required for data collection.

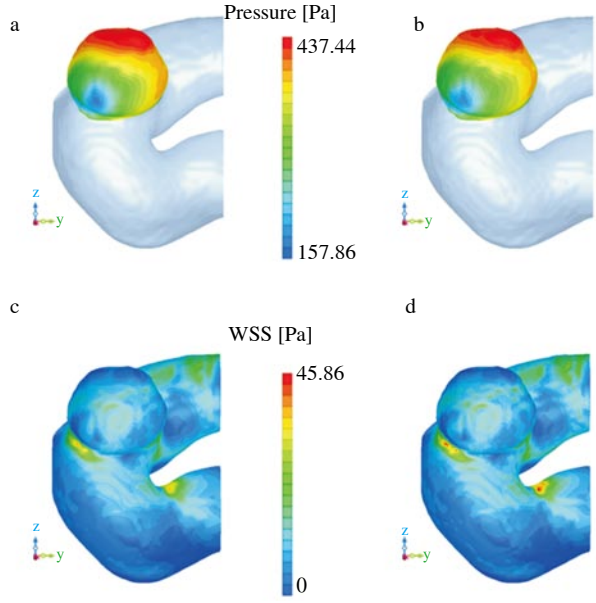

Figure 5. Time-averaged pressure distribution: a: Coarse mesh; b: Fine mesh and WSS distribution: c: Coarse mesh; d: Fine mesh.

3. Results

3.1. Time-averaged intraaneurysmal flow patterns

Time-averaged analysis, which was based on 5000 instantaneous data files in the fifth cycle, was performed for the three cases. The blood flow patterns inside the aneurysmal sac were compared in Figure 6. Complex vortex-like flows were observed inside the aneurysm for all three cases. Three represented streamlines were displayed for purposes of illustration. The black line indicates the fraction of the flow bypassing the aneurysm while the red and blue lines show the fraction of the blood entering into the aneurysmal sac. For the original anatomic aneurysm, the blood stream enters the aneurysm from the ostium and moves along the back left wall of the sac from the current view of the aneurysm as shown in Figure 6a. Then, after the bloodstream reaches the dome, a quantity of bloodstream keeps flowing along the right side wall and moving out, whereas a large amount of bloodstream turns down along the front surface resulting in vortices about the center of the aneurysmal

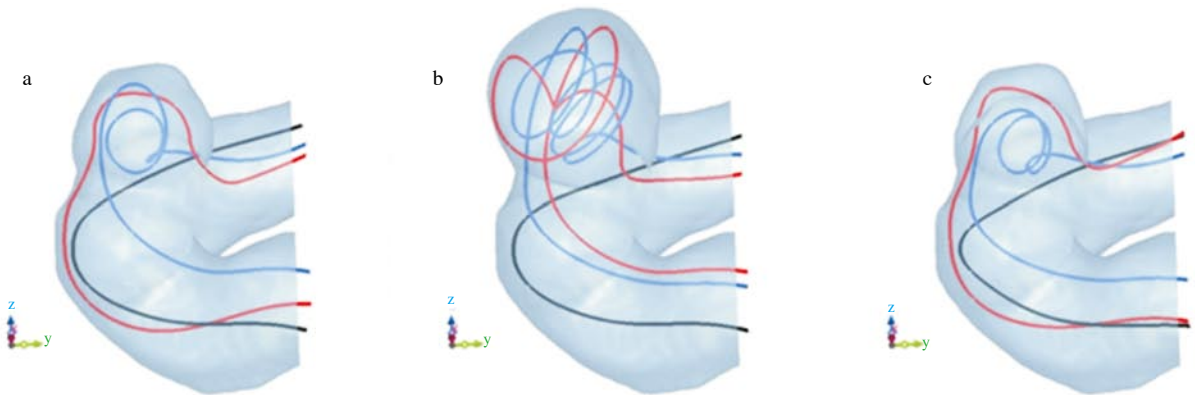

Figure 6. Time-averaged streamlines: a: The anatomic case; b: The enlarged case; c: The bi-lobed case.

sac, and then moves out of the aneurysm resulting in a spiral-line path.

Dissimilar to the anatomic case, the enlarged model generates a more complicated flow pattern inside the aneurysmal sac, as shown in Figure 6b. There is no bloodstream directly leaving the aneurysmal sac after reaching the dome. All flow turns down along the front surface generating large-scale, central, vortices which make the blood residence time longer. This results in an evenly low velocity distribution inside. The phenomenon can also be explained by linking with mass flow rate entering the aneurysm, which will be presented in the following. As performed in Figure 6c, the flow pattern of the bi-lobed case is similar to the anatomic model. Since the geometry has been changed, the dome of the aneurysm is now lower than the anatomic case so that the vortex is remained at a lower position compared to Figure 6a. Thus, the blood residence time is shorter than the anatomic case.

Figure 7 shows the time averaged velocity contour and 2D vector on the cross section of the ostium as shown in the Figure 7a. In order to illuminate the mass flow rate going into/out of the aneurysm, the velocity component normal to the cross section was used to compute the mass flow rate. As Figures 7b, 7c, and 7d presented, local high positive and negative out-of-plane velocities are observed in the anatomic and bi-lobed cases, which indicates more friction can be generated on the ostium region. The anatomic case had the largest mass flow rate (34.12%) out of the three cases, while the enlarged case had the lowest flow rate (23.78%). Therefore, under the same flow condition in the vessel, the increase of the aneurysmal sac volume gave rise to the decrease in velocity inside, which resulted in a lower WSS distribution on the surface of sac. In order to illuminate the details inside of the aneurysmal sac, several cut-planes with in-plane velocity vectors and out-of-plane velocity contours have been added, as shown in Figures 8, 9 and 10. The distance in-between the cut-planes is about 1.6 mm. Again, the bloodstream entering into the aneurysm is mainly from the left side, near the front surface from the present perspective, and moves out from the right side near the front surface. The high speed inflow and outflow around these two locations respectively could induce the local high WSS.

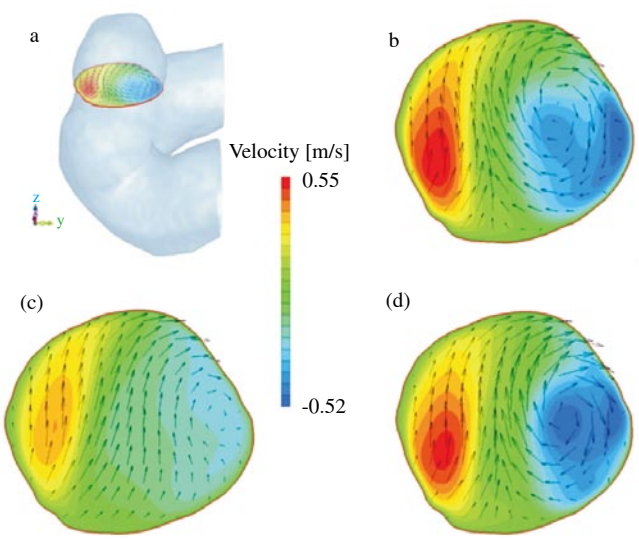

Figure 7. Time-averaged out-of-plane velocity contour with 2-D in-plane velocity vectors on the cross-section at the inlet of the aneurysm: a: 3D view of inlet of the aneurysm; (b) the anatomic case; (c) the enlarged case; (d) the bi-lobed case. Note that the range of the length of the velocity vector is from 0 to 0.38 m/s.

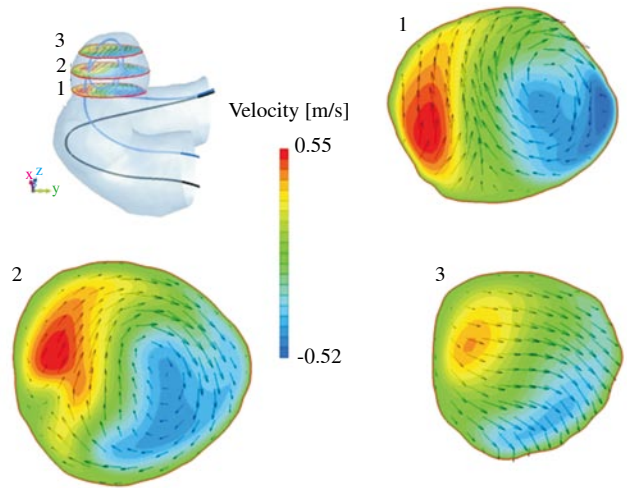

Figure 8. Time-averaged out-of-plane velocity contour with in-plane velocity vectors on several cross sections in the aneurysm with streamlines for the anatomic case.

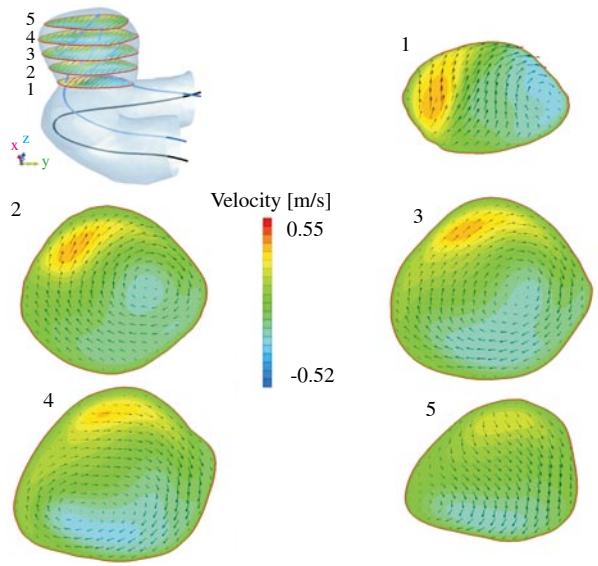

Figure 9. Time-averaged out-of-plane velocity contour with in-plane velocity vectors on several cross sections in the aneurysm for the evenly enlarged case.

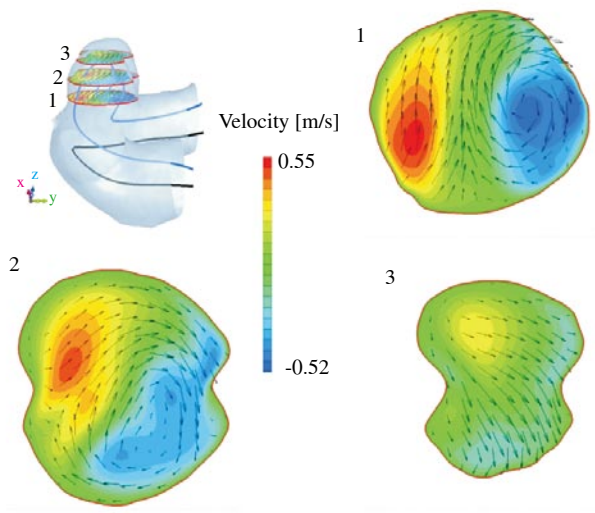

Figure 10. Time-averaged out-of-plane velocity contour with in-plane velocity vectors on several cross sections in the aneurysm with streamlines for the bi-lobed case

3.2. Pressure and WSS distribution of time-averaged analysis

Based on the time-averaged CFD simulation for the three models, pressure, WSS and their corresponding oscillatory components were extracted and mapped on the surface of the internal carotid aneurysm as shown in Figures 11, 12, 13, and 14, respectively. The WSS is calculated using the definition equation of the WSS, as presented in Eq. (1),

$$WSS=\tau_w=\mu\left.\frac{\partial u_T}{\partial n}\right|_{n=0} \quad (1)$$

where u_T is the velocity tangential to the local surface, n is the local coordinate normal to the local surface, and μ is the dynamic viscosity of the fluid. The variances of pressure and WSS provide information for the strength of the oscillation and are defined as $\sqrt{\overline{p'^2}}$ and $\sqrt{\overline{\tau_w'^2}}$ where prime denotes the difference between instantaneous and mean values and bar indicate average over one time cycle.

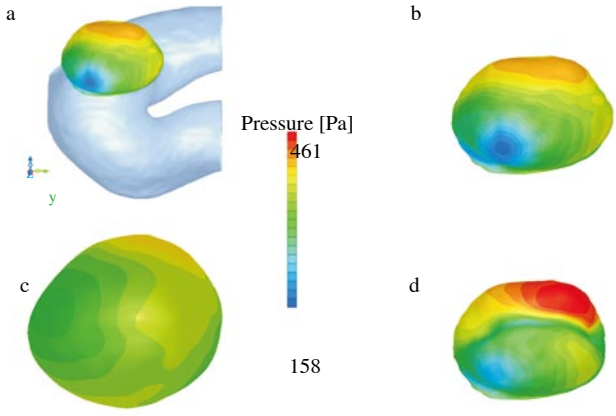

Figure 11. Time-averaged pressure distributions: a: The perspective of the aneurysm; b: The anatomic case; c: The enlarged case; d: The bi-lobed case.

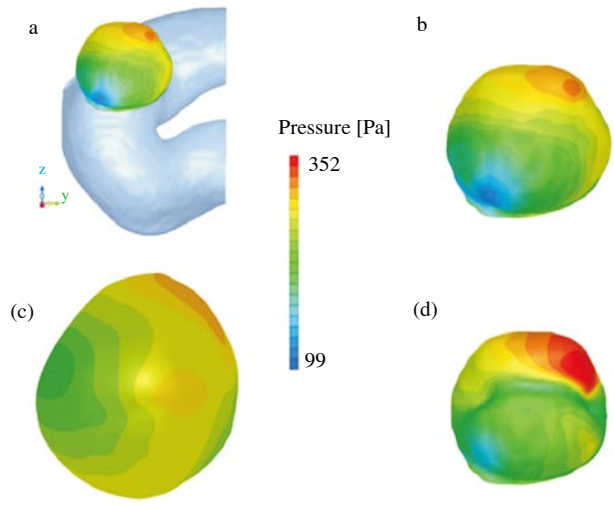

Figure 13. The root mean square of pressure distributions: a: The anatomic case; b: The enlarged case; c: The bi-lobed case.

The time-averaged pressure contours on the surface of the aneurysmal sac are presented in Figure 11, with Figure 11a showing the perspective view of the aneurysm. As shown in Figure 11b, the maximum pressure of 415.38 Pa on the anatomic model appears at the dome region in relation with the impingement, and the minimum pressure 157.62 Pa is located on the left hand side corresponding to the high speed passing flow. Figure 11c shows the pressure contour of the enlarged phantom morphology, the range of pressure is from 231.84 to 399.58 Pa. It has been observed that the range was dramatically narrowed compared to the anatomic model and thus the pressure is more uniformly distributed. The pressure contour for the bi-lobed phantom morphology is shown in Figure 11d. The range of pressures was from 158.84 to 461.00 Pa and a wider high pressure region is mainly concentrated in the concave region as compared to the original anatomic case.

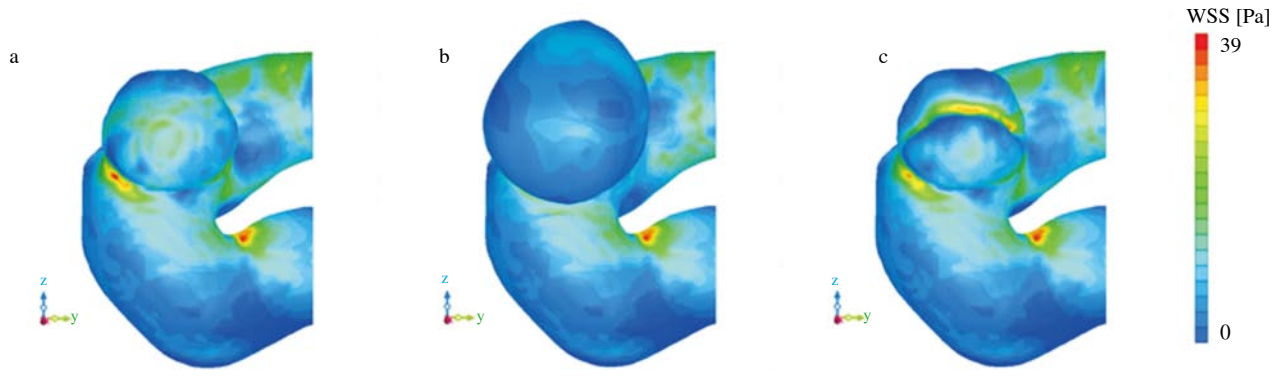

Figure 12. Time-averaged WSS distributions: a: The anatomic case; b: The enlarged case; c: The bi-lobed case.

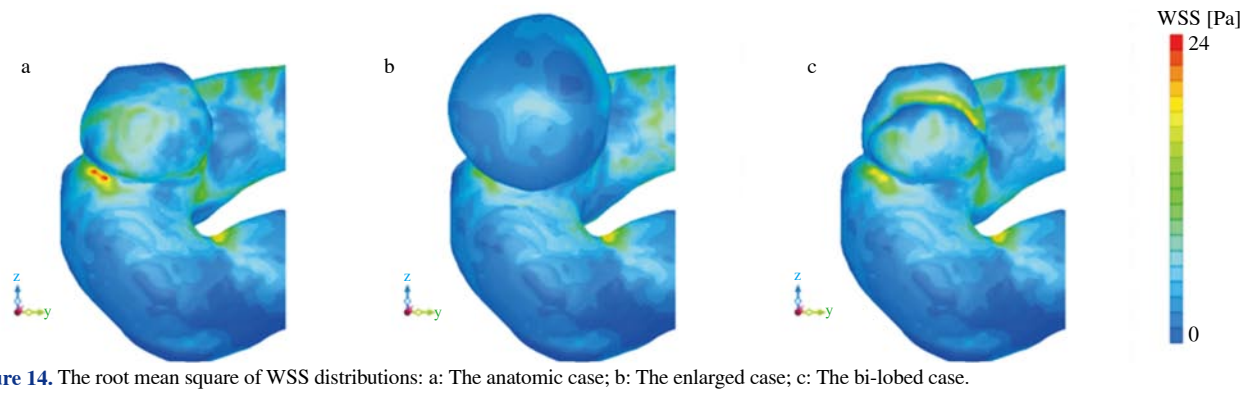

Figure 14. The root mean square of WSS distributions: a: The anatomic case; b: The enlarged case; c: The bi-lobed case.

Attention is now focused on the comparison of the WSS, as shown in Figure 12. For the original anatomic case as shown in Figure 12a, the maximum WSS of 39.05 Pa was observed at the aneurysm neck region as predicted in the previous analysis on the left hand side. On the sac surface, a maximum WSS of 17.61 Pa was observed in several places in the dome area. In contrast, WSS for the enlarged and bi-lobed cases are shown in Figures 12b and 12c, respectively. The distribution of WSS for the enlarged case become more uniform on the aneurysmal sac surface and it had a smaller magnitude (the maximum WSS was 9.81 Pa on the sac surface), which agreed with the previous analysis based on the flow characteristics. For the bi-lobed case, in addition to the regions close to the aneurysm neck, high WSS was also observed close to the aneurysm neck and the concave region on the dome, which also agreed with the previous estimation based on the flow characteristics. In this case, due to the irregularity of the aneurysm, there existed a region of high WSS near the concave region, having a maximum WSS of 33.20 Pa.

The contours for the root mean square of WSS are shown in Figures 13 and 14. It can be seen that the root mean quare of pressure and WSS is around 30.9% and 62.5% of the mean, and the contour distributions were similar to those of the mean pressure and WSS. The high root mean square value indicated that WSS is subject to a substantial oscillation due to the unsteady nature of the cardiac blood flow. The similarity in contours of the mean WSS and the root mean quare value implied that the region of impact caused by the unsteady nature was essentially in accordance with the area where large mean WSS was observed.

4. Discussion

CFD studies in the present study have assumed the same heart rate (HR) and blood pressure (BP), which represents a snapshot of the varying physiological conditions. However, by eliminating the effect of HR and BP, the present study presents a more pure influence of the morphology of the bleb aneurysm on the flow pattern, pressure and WSS distribution. In the present study, the 3D patient-specific UIA was successfully reconstructed and modeled for the CFD simulation. The saccular side-wall intracranial aneurysm in the present study belongs to the small bleb aneurysm phenotypes based on the classification of Meng *et al*[18]. The arterial flow characteristics are illustrated in terms of velocity vectors and streamlines. High velocity streams entered the aneurysm sac from the left back side, and became complex vortices. The high and unsteady pressure and friction on the arterial wall could induce a mural-cell-mediated pathway. It has been indicated that pressure elicits tensile stresses in the wall, which are felt by vascular mural cells, namely smooth muscle cells and fibroblasts[18]. Under unbalanced stresses, these mural cells can regulate collagen dynamics by cross-linking and synthesizing new collagen and degrading old collagen. Meanwhile, endothelial cells lining the vessel lumen sense changes in WSS from blood flow and transduce these mechanical signal into biologic signals, activating pathways to maintain vascular homeostasis. Through endothelial cell-mediated biology, WSS not only regulates vascular tone but also drives vascular remodeling under sustained deviations from physiologic baselines[25-28].

In the bi-lobed phantom morphology, the increased WSS observed on the sac surface associated with a higher flow velocity gradient and increased pressure could accelerate the process of the artery wall degeneration and weakening in response to changing hemodynamic loading and biomechanic stressors[29]. This situation is aggravated by the large unsteady nature of blood flow. The computational results showed that the oscillation of WSS essentially coincide with high averaged WSS. The changes in the aneurysmal wall properties could induce intensive strain especially near the margin between the stiff region and normal region, and cause the aneurysm to grow unevenly. The uneven feature of the aneurysm and high WSS are mutually caused and intensified. This trend could theoretically lead to the rupture of the aneurysm.

In the evenly enlarged phantom morphology, the decreased pressure and WSS on the sac surface are considered favorable for maintaining vascular homeostasis. However this is based on the hypothesis that the aneurysm is a thin-walled, smooth, hypocellular aneurysm phenotype. If it is a large, thick-walled, atherosclerotic aneurysm phenotype, the low WSS and high oscillatory shear could trigger an inflammatory-cell-mediated pathway, which could be associated with the growth and rupture of this type of aneurysm[17,30]. Such findings highlight aneurysm hemodynamics, in conjunction with better classification of aneurysms, could help determine the rupture of cerebral aneurysms.

Several limitations have impact on the accuracy of the results. In the CFD simulation, a rigid wall was applied because of the lack of information of arterial wall properties such as elasticity and thickness. The thickness of the bleb aneurysm is commonly thinner than an arterial wall, which is a possible factor for rupture. The averaged intra-arterial mass flow rate waveform is based on a total human intravascular network simulation. However, the unsteady physiological conditions such as the change of HR and BP were not taken into account in the present study. However, it is difficult to measure the precise waveform of a patient, because of different heart beats, total length of blood vessel, and the blood vessel structure. Based on this information, more accurate inlet boundary conditions and more precise fluid-structure interactions will be taken into account in our future studies.

An anatomic un-ruptured aneurysm on the ICA, and two phantom morphology models under the same inlet flow waveform were analyzed using CFD. The present study shows it is the intracranial aneurysm morphology and hemodynamics which have significant impact on pressure and WSS distribution on the surface of the cerebral aneurysm and not necessarily the overall size of the intracranial aneurysm. The predictions of rupture merely based on size of the aneurysm are questionable. Our research suggests that in the evenly enlarged phantom morphology, the decreased pressure and WSS on the sac surface are considered favorable for maintaining vascular homeostasis of a bleb aneurysm, while irregular morphologies of a small bleb aneurysm, such as bi-lobed configurations, could accelerate the process of the artery wall fibrosis which might lead to a higher risk of rupture.

Conflict of interest statement

We declare that we have no conflict of interest.

Acknowledgements

The authors would like to acknowledge the Translational Research Development Grants from the Office of Research Affairs in Wright State University, and the continued support of Premier Health with furthering the academic understanding with neuroscience.

References

[1] van Gijn J, Kerr RS, Rinkel GJ. Subarachnoid haemorrhage. *Lancet* 2007; **369**(9558): 306-318.

[2] Brinjikji W, Kallmes DF, Lanzino G, Cloft HJ. Hospitalization costs for endovascular and surgical treatment of ruptured aneurysms in the United States are substantially higher than Medicare payments. *AJNR Am J Neuroradiol* 2012; **33**(6): 1037-1040.

[3] Wiebers DO, Whisnant JP, Huston J 3rd, Meissner I, Brown RD Jr, Piepgras DG, et al. Unruptured intracranial aneurysms: natural history, clinical outcome, and risks of surgical and endovascular treatment. *Lancet* 2003; **362**(9378): 103-110.

[4] Cebral JR, Castro MA, Appanaboyina S, Putman CM, Millan D, Frangi AF. Efficient pipeline for image-based patient-specific analysis of cerebral aneurysm hemodynamics: technique and sensitivity. *IEEE Trans Med Imaging* 2005; **24**(4): 457-467.

[5] Berg P, Stucht D, Janiga G, Beuing O, Speck O, Thevenin D. Cerebral blood flow in a healthy Circle of Willis and two intracranial aneurysms: computational fluid dynamics versus four-dimensional phase-contrast magnetic resonance imaging. *J Biomech Eng* 2014; doi: 10.1115/1.4026108.

[6] Jou LD, Quick CM, Young WL, Lawton MT, Higashida R, Martin A, et al. Computational approach to quantifying hemodynamic forces in giant cerebral aneurysms. *AJNR Am J Neuroradiol* 2003; **24**: 1804-1810.

[7] Steinman DA, Milner JS, Norley CJ, Lownie SP, Holdsworth DW. Image-based computational simulation of flow dynamics in a giant intracranial aneurysm. *AJNR Am J Neuroradiol* 2003; **24**: 559-566.

[8] Ma B, Harbaugh RE, Raghavan ML. Three-dimensional geometrical characterization of cerebral aneurysms. *Ann Biomed Eng* 2004; **32**(2): 264-273.

[9] Shojima M, Oshima M, Takagi K, Torii R, Hayakawa M, Katada K, et al. Magnitude and role of wall shear stress on cerebral aneurysm: computational fluid dynamic study of 20 middle cerebral artery aneurysms. *Stroke* 2004; **35**(11): 2500-2505.

[10] Omodaka S, Sugiyama S, Inoue T, Funamoto K, Fujimura M, Shimizu H, et al. Local hemodynamics at the rupture point of cerebral aneurysms determined by computational fluid dynamics analysis. *Cerebrovasc Dis* 2012; **34**(2): 121-129.

[11] Cebral JR, Mut F, Weir J, Putman C. Quantitative characterization of the hemodynamic environment in ruptured and unruptured brain aneurysms. *AJNR Am J Neuroradiol* 2011; **32**: 145-151.

[12] Mantha A, Karmonik C, Benndorf G, Strother C, Metcalfe R. Hemodynamics in a cerebral artery before and after the formation of an aneurysm. *AJNR Am J Neuroradiol* 2006; **27**: 1113-1118.

[13] Cebral JR, Hendrickson S, Putman CM. Hemodynamics in a lethal basilar artery aneurysm just before its rupture. *AJNR Am J Neuroradiol* 2009; **30**: 95-98.

[14] Castro MA, Putman CM, Sheridan MJ, Cebral JR. Hemodynamic patterns of anterior communicating artery aneurysms: a possible association with rupture. *AJNR Am J Neuroradiol* 2009; **30**: 297-302.

[15] Castro M, Putman C, Radaelli A, Frangi A, Cebral J. Hemodynamics and rupture of terminal cerebral aneurysms. *Acad Radiol* 2009; **16**(10): 1201-1207.

[16] Avolio A, Farnoush A, Morgan M, Qian Y. Hemodynamic models of cerebral aneurysms for assessment of effect of vessel geometry on risk of rupture. *Conf Proc IEEE Eng Med Biol Soc* 2009; **1**: 2351-2353.

[17] Cebral JR, Castro MA, Burgess JE, Pergolizzi RS, Sheridan MJ, Putman CM. Characterization of cerebral aneurysms for assessing risks of rupture by using patient-specific computational hemodynamics models. *AJNR Am J Neuroradiol* 2005; **26**(10): 2550-2559.

[18] Meng H, Tutino VM, Xiang J, Siddiqui A. High WSS and low WSS? Complex interaction of hemodynamics with intracranial aneurysm initiation, growth, and rupture: toward a unifying hypothesis. *AJNR Am J Neuroradiol* 2014; **35**: 1254-1262.

[19] Liang F, Takagi S, Himeno R, Liu H. Multi-scale modeling of the human cardiovascular system with applications to aortic valvular and arterial stenosis. *Med Biol Eng Comput* 2009; **47**: 743-755.

[20] Huang PG, and Muller LO. Simulation of one-dimensional blood flow in networks of human vessels using a novel TVD scheme. *Int J Numer Method Biomed Eng* 2014; doi: 10.1002/cnm.2701.

[21] Grodins FS. Integrative cardiovascular physiology: a mathematical synthesis of cardiac and blood vessel hemodynamics. *Q Rev Biol* 1959; **34**(2): 93-116.

[22] Hales S. *Statistical essays: containing hemostaticks, or an account of some hydraulick and hydrostatical experiments on the blood and blood-vessels of animals*. London: Innys & Manby; 1733.

[23] Frank O. Die grundform des arterielen pulses: Erste abhandlung. Mathematische analyse. *Mamm Biol* 1899; **37**: 485-526.

[24] Kokalari I, Karaja T, Guerrisi M. Review on lumped parameter method for modeling the blood flow in systemic arteries. *J Biomed Sci Eng* 2013; **6**(1): 92-99.

[25] Humphrey JD, Taylor CA. Intracranial and abdominal aortic aneurysms: similarities, differences, and need for a new class of computational models. *Annu Rev Biomed Eng* 2008; **10**: 221-246.

[26] Nixon AM, Gunel M, Sumpio BE. The critical role of hemodynamics in the development of cerebral vascular disease. *J Neurosurg* 2010; **112**(6): 1240-1253.

[27] Metaxa E, Tremmel M, Natarajan SK, Xiang J, Paluch RA, Mandelbaum M, et al. Characterization of critical hemodynamics contributing to aneurysmal remodeling at the basilar terminus in a rabbit model. *Stroke* 2010; **41**(8): 1774-1782.

[28] Kolega J, Gao L, Mandelbaum M, Mocco J, Siddiqui AH, Natarajan SK, et al. Cellular and molecular responses of the basilar terminus to hemodynamics during intracranial aneurysm initiation in a rabbit model. *J Vasc Res* 2011; **48**(5): 429-442.

[29] Cebral JR, Raschi M. Suggested connections between risk factors of intracranial aneurysms: a review. *Ann Biomed Eng* 2013; **41**(7): 1366-1383.

[30] Malek AM, Alper SL, Izumo S. Hemodynamic shear stress and its role in atherosclerosis. *JAMA* 1999; **282**(21): 2035-2042.